Prediction of Potential Dependent Kinetics for the Electrocatalytic Reduction of CO_2 to CO over Ti@4N-Gr

Yousef A. Alsunni[*,1,2], Abdulaziz W. Alherz[3], Charles B. Musgrave[*,2,4,5]

[1]Chemical Engineering Department, King Fahd University of Petroleum and Minerals, Dhahran 31261, Saudi Arabia

[2]Department of Chemical and Biological Engineering, University of Colorado Boulder, Boulder, CO 80309, USA

[3]Department of Chemical Engineering, College of Engineering and Petroleum, Kuwait University, Safat 13060, Kuwait

[4]Renewable and Sustainable Energy Institute, University of Colorado Boulder, Boulder, CO 80309, USA

[5]Materials Science and Engineering Program, University of Colorado Boulder, Boulder, CO 80309, USA

[*]Correspondence should be addressed to yalsunni@kfupm.edu.sa and charles.musgrave@colorado.edu

Abstract

Grand canonical density functional theory (GC-DFT) was employed to model the electrocatalytic reduction of CO_2 (CO_2R) to CO by single titanium atom nitrogen-doped graphene, referred to as Ti@4N-Gr. Previous GC-DFT thermodynamic investigations have identified Ti@4N-Gr as a promising CO_2R catalyst, however no in-depth studies have examined it. In this study, we analyze activation energies of the elementary steps at various applied potentials in addition to thermodynamics of CO_2R to CO catalyzed by Ti@xN-Gr defects. Reaction intermediates are predicted to be destabilized when Ti is coordinated to fewer N atoms. Based on reaction thermodynamics, Ti@4N-Gr and all defect configurations are predicted to be potentially promising catalysts for CO_2R to CO at an applied potential of -0.7 V_{SHE} while at -0.3 and -1.2 V_{SHE}

the reaction is predicted to be hindered by relatively large grand free energy differences between intermediates. We propose a criterion to identify optimum applied potentials for CO_2R to CO based on the potential of zero charge (PZC) of the reaction intermediates and the contention that the optimum applied potential for CO_2R to CO lies in the range $PZC_{*CO} < V < PZC_{*CO_2^-}$ that can be generalized to other electrocatalytic systems. Solvating H_2O molecules form strong hydrogen bonds with the *COOH intermediate, especially at more oxidizing potentials, which increases the energetic costs required for the protonation of *COOH by 0.18 to 0.43 eV at applied potentials of -1.2 to -0.3 V_{SHE}. Grand canonical nudged elastic band (GC-NEB) was used to predict the activation barriers of CO_2R to CO catalyzed by Ti@4N-Gr. GC-NEB predicts that all activation barriers along the reaction pathway are potential-dependent, where CO desorption and CO_2 adsorption have the largest barriers at highly reducing and highly oxidizing potentials, respectively.

Keywords: grand canonical density functional theory, electrocatalysis, carbon dioxide reduction, nudged elastic band, surface reaction, transition state, 2d materials

Introduction

Carbon dioxide (CO_2) is a significant contributor to global warming that is emitted as a byproduct across nearly every sector of modern industry.[1-6] The imperative to combat climate change has led to a growing interest in recycling CO_2 into value-added products, an integral part of closed loop solutions that not only meet rising demand for valuable carbon-based products but also align with the goal of achieving net-zero carbon emissions.[7-13] The conversion of CO_2 into

value added products presents several challenges, including the high stability of CO_2, the need for high product selectivity, and the necessity to lower process costs.[14-19] Among the various approaches, electrochemical CO_2 reduction (CO_2R) to carbon monoxide (CO) emerges as an attractive option. This method has the potential to achieve Faradaic efficiencies exceeding 95%. However, the successful implementation of electrocatalysis on an industrial scale is hindered by its reliance on expensive catalysts.[20-23]

Alternative electrocatalysts for CO_2R to CO include two-dimensional single metal atom nitrogen doped carbon (M@N-Gr) materials. In M@N-Gr materials, a metal center (M) serves as the catalytically active site and is bound to one or more nitrogen atoms of N-doped graphene.[24] M@N-Gr catalysts have demonstrated remarkable selectivity, producing CO with observed Faradic efficiencies of up to 95%.[25-31] Among the synthesized M@N-Gr catalysts, the square-planar M@4N-Gr catalysts, characterized by pyridinic coordination of the metal by four nitrogen atoms, has been reported as the most stable.[31-32]

The computational hydrogen electrode (CHE) model has been widely employed to approximate the influence of the applied potential on electrochemical reactions by correcting energies computed by density functional theory (DFT).[33-41] The CHE method adjusts the energies of proton coupled electron transfer (PCET) steps computed by DFT by an amount that depends linearly on the applied potential. While the CHE method is simple and elegant, it can be inaccurate because it does not consider the variation of the number of electrons nor the geometry of the reacting species with changing applied potential.[42-44] An alternative is to directly model the effects of the electrified interface on the electronic structure of the reacting system. Grand canonical density functional theory (GC-DFT) accomplishes this by solving the electronic structure problem at a fixed applied electrode potential by self-consistently calculating the number of electrons in the

system for that potential. Additionally, it predicts changes in the geometries of intermediates and transition states (TS) due to the applied potential by calculating forces from the dependence of the grand free energy on the atomic positions.[45-48]

We previously used GC-DFT to investigate the electrochemical reduction of CO_2 to CO catalyzed by pyridinic M@4N-Gr catalysts, where M is a first-row transition metal bound to four pyridinic N atoms of N-doped graphene. In our study, Ti@4N-Gr emerged as a promising catalyst for this conversion, as indicated by the GC-DFT-computed thermodynamics of the reaction steps.[43] However, our study's focus was primarily on screening the first-row 3d metal centers of pyridinic M@4N-Gr materials to identify potential catalysts for CO_2R to CO based on GC-DFT-computed thermodynamic reaction coordinate diagrams – that is, based on the energies of the reaction steps without calculating the activation barriers. Therefore, an extension of that study is warranted to comprehensively evaluate Ti@4N-Gr effectiveness as an electrocatalyst for CO_2R to CO, especially considering the limited existing research on Ti@4N-Gr as a catalyst. The synthesis of Ti@4N-Gr has been documented in several studies.[49-50] However, to date, there are no reported experimental investigations using this material specifically as a catalyst for CO_2 reduction. Nevertheless, the applicability of Ti-doped graphene has been explored in various first-principles studies, demonstrating its potential in several catalytic processes. For instance, research has highlighted its utility in water splitting[51], CO oxidation[52], the formation of formic acid[53], and the sensing of toxic gases[54-56]. These studies collectively underscore the promising nature of Ti-doped graphene in various catalytic applications, despite the lack of direct evidence for its role in CO_2 reduction. To address this gap, our extended study encompasses several aspects, including the examination of the stability of the Ti atom within the N-doped graphene sheet under varying applied potentials, exploration of the reaction pathways at defects in Ti@xN-Gr catalysts that

might be formed during catalyst synthesis, an investigation into the influence of hydrogen bonding on reaction intermediates, and the computation of activation barriers as a function of the applied potential.

In this report, we employed GC-DFT to investigate the electrocatalytic conversion of CO_2 to CO on Ti@4N-Gr. Our approach began with an assessment of the stability of the Ti center under various applied potentials using GC-DFT. Additionally, we computed the optimum distance between the Ti atom and the Ti@4N-Gr sheet. To comprehensively explore the reaction pathway, we utilized the grand canonical-nudge elastic band (GC-NEB)[57] method to calculate TS energies for all elementary reaction steps involved in CO_2R to CO over Ti@4N-Gr. Furthermore, our study extended to CO_2R to CO over Ti@xN-Gr defects, where the metal center is coordinated to x = 1, 2, or 3 nitrogen atoms. We also delved into the thermodynamic factors that govern CO_2R to CO over Ti@4N-Gr to determine conditions that make it thermodynamically feasible at specific potentials. To aid in the selection of an ideal applied potential range for CO_2R to CO, we propose a criterion based on the potential of zero charge (PZC) of the reaction intermediates. Finally, we examined the effects of hydrogen bonding between solvating water molecules and various reaction intermediates and TSs throughout all elementary reaction steps under various applied potentials.

Methods

Energy Equations and Reaction Coordinate Diagram

The energies of states along the reaction coordinate diagrams are plotted relative to the energies of a reference species. In the case of CO_2R to CO, it is convenient to choose the product state at infinite separation as the thermodynamic reference. This enables the calculation of grand free energies of intermediates, TSs, and the initial reactants at each applied potential by subtracting

their grand free energies from those of the reference species. The specific equations used for the calculations are given in the **Supporting Information**.

Computational Details

Ti@4N-Gr sheets were modeled as supercells each containing 44 C atoms, 4 N atoms and 1 Ti atom with approximate dimensions of 12 Å×12 Å×23 Å, which corresponds to a distance of >22 Å separating periodic images of the sheet along the vertical direction. This unit cell was sampled using a 3×3×1 Γ-point centered k-point grid. The Monkhorst Pack algorithm was used to select the k-point meshes of all slabs.[58]

GC-DFT calculations were performed using the joint density functional theory (JDFTx) code,[59] the PBE-D3 exchange-correlation functional, GBRV pseudopotentials and a plane wave basis with a 20 Hartree cutoff energy. Fermi-Dirac smearing with a 0.001 Hartree width was used to accelerate the self-consistent field convergence. Electronic structure calculations were converged to a threshold of 1×10^{-8} Hartree, while geometry optimizations were converged to a threshold of 1×10^{-4} Hartree. The charge-asymmetry corrected, local-response and nonlocal-cavity (CANDLE) solvation model was employed to treat solvation effects on charged/adsorbed species and maintain the neutrality of charged surfaces in the unit cell.[60] Following the convergence of the electronic wavefunction in each SCF cycle, the CANDLE solvent model iteratively solves for the charge distribution in the solvent as a response to the solute's (surface's) updated charge distribution until a charge-neutral unit cell is achieved. The algorithm is described in much more detail in the article describing the GC-DFT formalism.[61] The GC-DFT method describes the effect of the applied bias on the reaction by self-consistently minimizing the grand free energy while solving for the number of electrons that results in a Fermi level, that is the chemical potential of electrons (μ), that matches the applied potential. We are interested in understanding the behavior

of Ti@4N-Gr under mildly reducing (-0.3 V_{SHE}), moderately reducing (-0.7 V_{SHE}), and strongly reducing conditions (-1.2 V_{SHE}). Details of the computational settings and atomic positions are available in the **Supporting Information.**

Grand-Canonical Nudged Elastic Band Approach

The JDFTx base calculator was implemented within the pythonic atomic simulation environment (ASE)[62] to enable its use with the ASE implementation of the NEB method.[57, 63-64] This enables the calculation of each NEB image, independent charge density and solvent response at the specified applied potential. In this work, we implemented the GC-NEB[57] approach to calculate TSs of all elementary steps of the CO_2R to CO mechanism as a function of the applied potential. GC-NEB refers to the NEB algorithm in which forces are calculated using GC-DFT for each iteration, allowing the number of electrons to vary while the chemical potential remains constant, thereby determining the transition state energy at a constant potential. For the TS of each elementary step, a minimum of five images (not including the initial and final states) was used to obtain the minimum energy pathway (MEP) and the grand free activation energies (Φ_a), which were calculated as the differences between the grand free energies of each TS and the initial state. The grand free energy of the TS is defined as the maximum energy along the MEP, as represented by converged NEB images.

Results and Discussion

Stability of the Ti@4N-Gr Site under Different Applied Potentials

We first calculate the formation energy of Ti@4N-Gr using its reference constituents: graphite, N_2, and bulk Ti metal. The energy required to form a supercell, which contains 44 carbon atoms, 4 nitrogen atoms, and 1 Ti atom, is 1.31 eV. This value is significantly lower than the 6.41 eV required to form a similar-sized supercell of the experimentally synthesized RuN_2C, suggesting that Ti@4N-Gr should be synthesizable.[65] Furthermore, we assess the stability of the Ti center within the Ti@4N-Gr site at various applied potentials before investigating its catalysis of CO_2R. **Figure 1** plots the computed total grand free energies of the supercell model of the Ti over N-doped graphene sheet at various distances of the Ti atom from the sheet. These results show that at applied potentials of -0.3, -0.7, and -1.2 V_{SHE}, the optimum geometry for Ti@4N-Gr is a puckered structure with the Ti atom positioned 0.99 Å from the sheet. Additionally, the plot shows that the Ti atom in the Ti@4N-Gr site is stable across all applied potentials. The carbon and the nitrogen atoms of the optimized geometry lie in the same horizontal plane. This suggests that the supercell model used is of a sufficient size to accurately simulate reactions at the isolated Ti@4N-Gr site of an M@N-GR sheet.

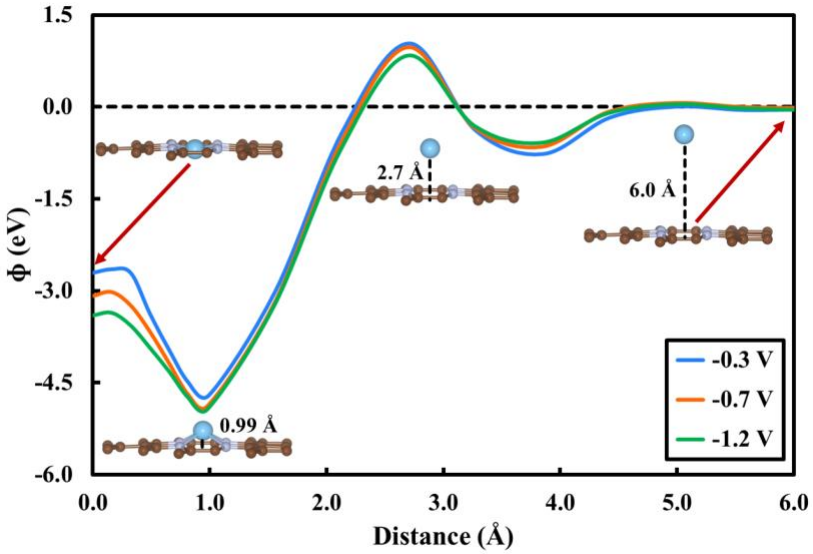

Figure 1: Energy profile for the Ti atom placed at different distances from the 4N-Gr ~~N_4C~~ sheet. All grand free energies are calculated relative to the infinite separation between the Ti atom and the other atoms of the 4N-Gr sheet. All voltages are relative to the standard hydrogen electrode (SHE). The most stable geometry is obtained for the puckered structure where the Ti atom lies 0.99 Å above the sheet. The Ti center of the Ti@4N-Gr site is stable at the three applied potentials considered.

Reaction Pathway of CO_2R to CO over Ti@4N-Gr

DFT studies of electrochemical processes commonly only consider the thermodynamics of the elementary reaction steps of a mechanism and ignore their activation barriers because of the computational expense associated with computing TSs. This is especially true for the barriers of reactions that occur in the presence of an applied electrical bias.[66] Therefore, we preformed GC-NEB calculations to predict the barriers for all elementary steps of CO_2R to CO over Ti@4N-Gr to investigate how the applied potential influences the barriers of the elementary steps, and thus the kinetics of the reaction. **Figure 2** plots the reaction coordinate diagram for CO_2R to CO catalyzed by Ti@4N-Gr at -0.3, -0.7 and -1.2 V_{SHE}, including activation barriers. GC-NEB predicts a relatively high activation energy of 1.02 eV for CO_2 adsorption at -0.3 V_{SHE}, but a considerably lower activation energy for this step at more reducing potentials such that CO_2 adsorbs at -0.7 V_{SHE}

with a moderate barrier of 0.87 eV. This results because the more negatively charged catalyst at more reducing potentials donates additional electron density through π backbonding to the π^* states (*C=O) of CO_2, which lowers the activation energy to form $*CO_2^-$. A recent study has shown that this barrier is significantly reduced when modeling the reaction with explicit cations.[67] The presence of cations plays a critical role in the CO_2R reaction, as they stabilize negatively charged species and enhance the accuracy of kinetic barrier calculations, ultimately influencing the efficiency and selectivity of the reaction. However, the role of explicit ions is beyond the scope of this work.

Following the adsorption of CO_2 on Ti@4N-Gr to form $*CO_2^-$, CO_2R to CO proceeds through the protonation of $*CO_2^-$ to form *COOH. In this study, we assume that the reaction occurs in an acidic medium, so hydronium (H_3O^+) is chosen as the proton donor to simulate the hydrogenation steps. Several studies suggest that H_3O^+ is a relevant proton source in the context of electrochemical reduction reactions due to its high proton conductivity and availability in acidic solutions.[68-70] However, activation barriers may be influenced by the choice of proton source, as different proton donors exhibit varying degrees of stability and reactivity, which can alter the energetics of the protonation steps. GC-DFT predicts that protonation of $*CO_2^-$ to form *COOH is barrierless and exergonic at the considered potentials, allowing $*CO_2^-$ to be readily converted to *COOH. This is because $*CO_2^-$ is a highly reactive and unstable species that tends to be protonated spontaneously. The prediction of a barrierless protonation step could be an artifact of using an implicit solvent that results in the under-solvation of H_3O^+. This has motivated some researchers to recommend the use of micro-solvated H_3O^+. [71-72] However, this is beyond the scope of this work.

The second protonation step to form *CO from *COOH is only limited by the grand free energy difference between these two intermediates at -0.3 V_{SHE}, calculated to be 0.85 eV. In contrast, GC-

NEB predicts activation barriers of 0.69 and 0.46 eV at -0.7 and -1.2 V_{SHE}, respectively. This results because hydrogen bonding stabilizes the transition state (TS_3 in **Figure 2**) more than the *CO intermediate state at -0.3 V_{SHE}. However, more reducing potentials increase the energy of *COOH and lower the energy of *CO. At -0.7 and -1.2 V_{SHE}, hydrogen bonding stabilizes *COOH and TS_3 less than at -0.3 V_{SHE} because at more reducing potentials the H atom of *COOH becomes less positive and hence bonds more weakly to the O atom of the water molecule. We calculated hydrogen bond strengths between *COOH and the explicit water molecule of 0.43, 0.33, and 0.18 eV for applied potentials of -0.3, -0.7, and -1.2 V_{SHE}, respectively. We also examined the effect of hydrogen bonding with an additional water molecule positioned to interact with *COOH and found only a minor stability increase of 0.07 eV at -0.3 V_{SHE}. This suggests that one explicit H_2O molecule, combined with the implicit solvent, adequately captures the influence of hydrogen bonding on reaction energetics.

The final step is the desorption of *CO, which GC-NEB predicts requires a large activation barrier of 0.90 eV at -0.3 V_{SHE} that increases to 0.95 and 1.28 eV at -0.7 and -1.2 V_{SHE}, making it the largest barrier at these potentials. However, at -0.3 V_{SHE} the largest activation barrier of this mechanism predicted by GC-NEB is CO_2 adsorption. This demonstrates a case of an electrochemical reaction where the rate determining step (RDS) is potential dependent. Moreover, the analysis also shows the significance of hydrogen bonding in that it stabilizes *COOH at more oxidizing potentials and consequently substantially increases the barrier to protonate *COOH. For comparison, **Figure S1** plots the full reaction coordinate diagram for CO_2R to CO over Ti@4N-Gr without considering hydrogen bonding effects.

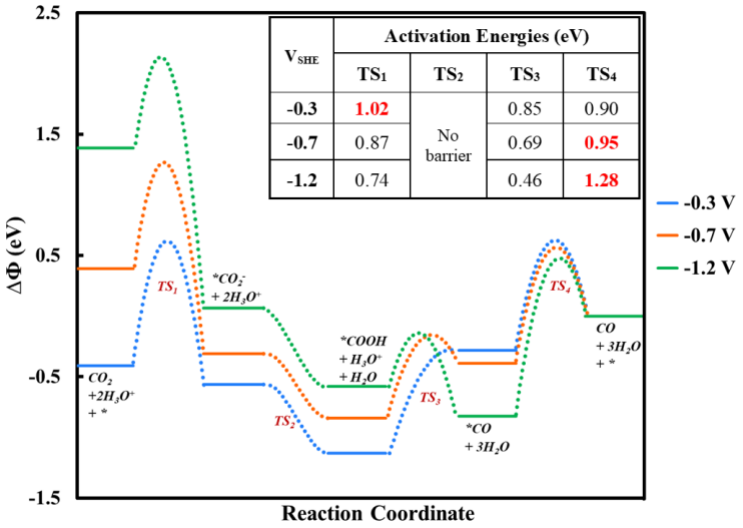

V_{SHE}	Activation Energies (eV)			
	TS_1	TS_2	TS_3	TS_4
-0.3	1.02	No barrier	0.85	0.90
-0.7	0.87		0.69	0.95
-1.2	0.74		0.46	1.28

*Figure 2: Full reaction pathway for CO_2R to CO on Ti@4N-Gr including all TSs and hydrogen bonding effects. The vibrational entropic contributions to the grand free energies of the adsorbates and the water molecule are included in the calculation. The inset table shows the activation energies for all TSs under the three potentials considered. The energies highlighted in red are the energies of the largest kinetic barriers. All barriers are affected by the applied potential. CO desorption (TS_4) has the highest barrier along the reaction pathway at -0.7 and -1.2 V_{SHE} and the barrier increases under more reducing potentials. However, the barriers for TS_1 and TS_3 diminish with more reducing potentials. *CO_2^- is extremely reactive and hence no barrier is associated with TS_2.*

The Optimum Applied Potential Range for CO_2R to CO

Selecting the optimum applied potential for any electrochemical process is a critical step. To determine the optimum applied potential range for a reaction it is helpful to understand how the applied potential influences the energetics of each step in the reaction. Thus, to predict the performance of Ti@4N-Gr for catalyzing CO_2R to CO we computed how the applied potential affects the reaction energetics and analyzed these results to identify an optimum applied potential.

An important factor that must be considered in evaluating electrocatalysis is the PZC of the system, which is the Fermi level (chemical potential of electrons) of the neutral (uncharged) system. The PZC can be calculated by canonical DFT, where the electron number is fixed, and the chemical potential (Fermi level) is determined accordingly. Commonly, applied potentials are referred to as

oxidizing or reducing relative to 0 V_{SHE}, which is the potential at which protons are reduced to H_2. However, a reducing potential (relative to 0 V_{SHE}) can still be oxidizing to a particular system if the system's PZC is more negative than the applied potential, and vice versa. In this work, we redefine reducing potentials as those that are less than the PZC, whereas oxidizing potentials are those greater than the PZC of a particular system. Note that a reducing potential can be positive (relative to 0 V_{SHE}) for positive PZCs and oxidizing potentials can be negative (relative to 0 V_{SHE}) for negative PZCs. The PZC is affected by interaction of the catalyst with adsorbates, and hence, each reaction intermediate that interacts with the electrocatalyst changes the PZC of the system.

Figure 3 plots the reaction coordinate diagram of the CO_2R to CO conversion showing the PZC of each reaction intermediate and the ranges of the oxidizing and the reducing potentials for each intermediate. Here, we computed the PZC for each intermediate at a coverage of one adsorbed intermediate per supercell. Thus, the computed PZC depends on the supercell size and assumes no other species adsorbed within the unit cell. The PZC of *CO is -0.84 V_{SHE}, and hence, any potential less negative than this value is an oxidizing potential. For Ti@4N-Gr, *CO is less stable under more oxidizing potentials. Consequently, GC-DFT predicts more facile desorption of *CO at potentials less negative than -0.84 V_{SHE}. This cause of the more facile desorption of *CO at the applied potentials of -0.3 and -0.7 V_{SHE} versus the high stability of *CO at -1.2 V_{SHE} is illustrated in **Figure 3**. **Figure 4** plots the projected density of states (PDOS) of the valence bands of Ti and CO adsorbed on the Ti@4N-Gr site at various applied potentials. **Figure 4 (c)** shows that the bonding states between CO and the Ti site lie just below the Fermi level at the PZC. Thus, electrons are removed from bonding states at potentials more oxidizing than the PZC, which weakens the bond between CO and Ti@4N-Gr site (**Figures 4 (a)** and **(b)**). However, **Figure 4 (d)** shows that

at potentials more reducing than the PZC electrons are added to the bonding states, which stabilizes the adsorption of CO on the Ti@4N-Gr site.

More reducing potentials tend to stabilize *CO and $*CO_2^-$. Thus, an optimum applied potential for CO_2R to CO catalyzed by Ti@4N-Gr is expected to be in the range $PZC_{*CO} < V < PZC_{*CO_2^-}$ – that is, -0.84 $V_{SHE} < V <$ -0.22 V_{SHE}. For this criterion to be valid, the geometries of *CO and $*CO_2^-$ must not significantly differ from their geometries at their respective PZCs. Significant changes in the geometry that influence the PZC usually involve breaking and/or forming of bonds between the adsorbate and the catalyst site. This criterion could be generalized to catalysts that stabilize *CO at more reducing potentials, which implies that $PZC_* < PZC_{*CO}$, where PZC_* is the potential of zero charge of the bare catalyst surface.

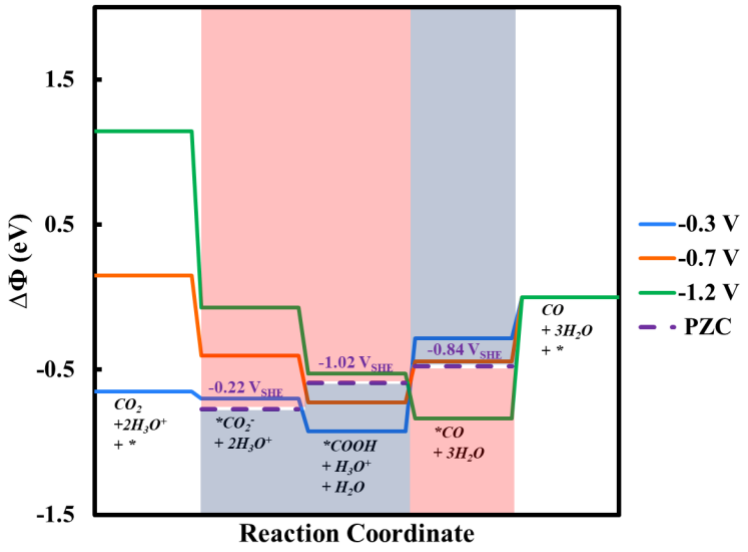

*Figure 3: Reaction coordinate diagram for CO_2R to CO over Ti@4N-Gr under different applied potentials. The dashed purple lines represent the PZCs of $*CO_2$, *COOH, and *CO where the energetics of all species included at each intermediate step are calculated based on the PZC. The red and blue shaded areas represent the ranges of grand free energies that result from reducing potentials more negative (red) or oxidizing potentials less negative (blue) than the PZCs of $*CO_2^-$, *COOH, and *CO. The optimum potential (V_{opt}) for CO_2R to CO should be in the range of* $-0.84 < V_{opt} < -0.22$ V_{SHE}. *i.e.,* $PZC_{*CO} < V < PZC_{*CO_2^-}$.

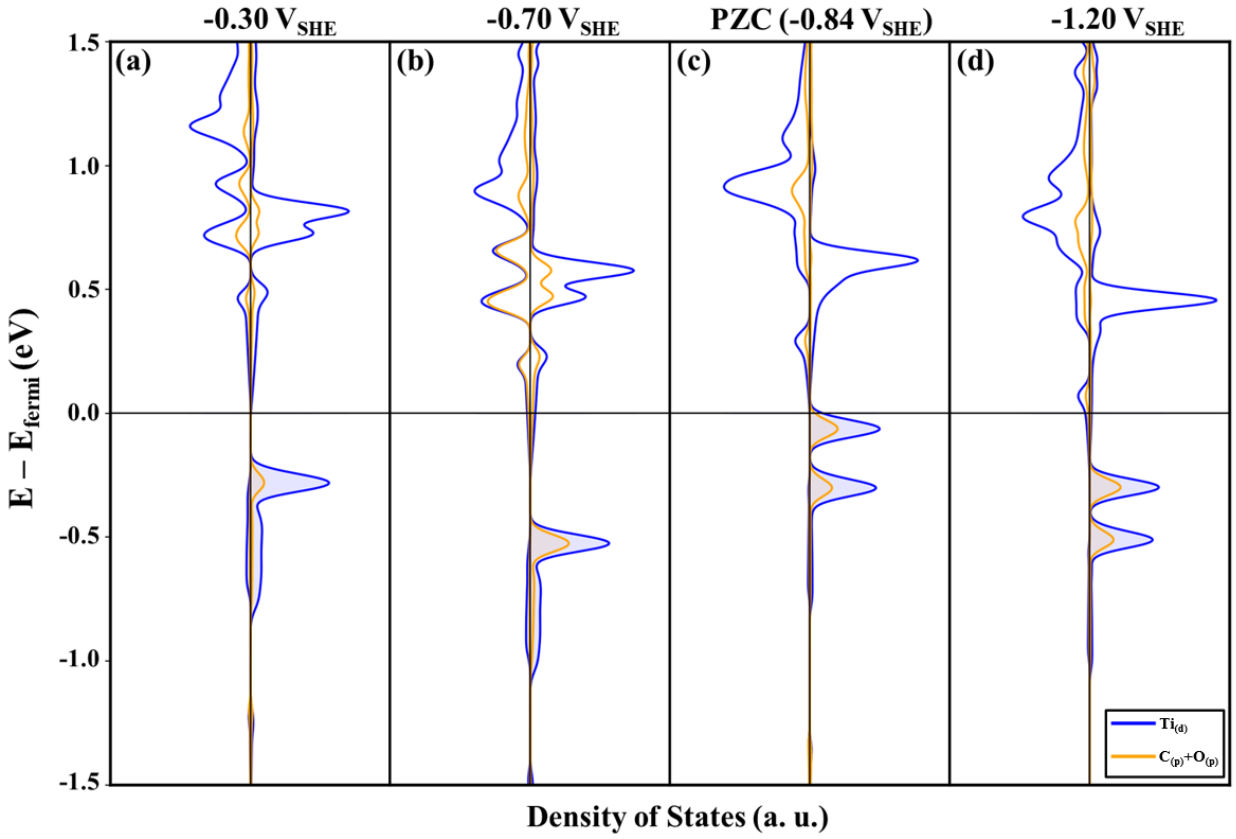

Figure 4: PDOS of the valence bands of Ti, C, and O of the adsorbed CO on the Ti@4N-Gr site within 1.5 eV of the Fermi level at (a) -0.3, (b) -0.7, (c) PZC, and (d) -1.2 V_{SHE}. The shaded areas indicate filled states. CO bonds stronger to the Ti@4N-Gr site at more reducing potentials as the bonding states are filled with electrons. In contrast, applying more oxidizing potentials removes electrons from bonding states and hence, weakens the bond between the Ti site and CO.

Effect of Hydrogen Bonding on Reaction Intermediates

The reduction of CO_2 to CO usually occurs in aqueous solvent in which water molecules stabilize the reaction intermediates through hydrogen bonding.[73] The three reaction intermediates $*CO_2^-$, *COOH and *CO hydrogen bond to water with different bond strengths, and will thus be stabilized to a differing degree by hydrogen bonding with solvating water molecules. Furthermore, $*CO_2^-$ and *CO hydrogen bond with water where their oxygen atoms hydrogen bond to a proton of a water molecule. In contrast, the proton of *COOH hydrogen bonds to an oxygen atom of a water

molecule. **Figure 5** plots the reaction coordinate diagram of the reduction of CO_2 to CO catalyzed by Ti@4N-Gr including hydrogen bonding with one explicit water molecule. The grand free energies reported in this plot include the entropic contributions at room temperature from the vibrations of the adsorbate and the explicit water molecule. The plot shows that the hydrogen bond strength between $*CO_2^-$ and H_2O is insensitive to the applied potential. However, more reducing potentials weaken the hydrogen bond between *COOH and H_2O because the proton of *COOH becomes less positive at more reducing potentials, which weakens the Coulombic attraction of this proton to the oxygen atom of the water molecule. On the other hand, the small electric dipole moment of *CO leads to a weak hydrogen bonding interaction with H_2O and thus negligible stabilization of *CO. *COOH is the reaction intermediate most sensitive to hydrogen bonding and is stabilized by 0.18 to 0.43 eV at applied potentials from -1.2 to -0.3 V_{SHE}, respectively. This stabilization increases the endothermicity of the second protonation step ($* COOH + H^+ + e^- \rightarrow CO + H_2O$) by 0.85 eV at an applied potential of -0.3 V_{SHE}, whereas it is uphill by only 0.42 eV at this applied potential in the absence of hydrogen bonding to an explicit water molecule. This indicates that the reaction will likely not proceed at room temperature for potentials less reducing than -0.3 V_{SHE}, which would not be predicted in the absence of hydrogen bonding. However, at -0.7 V_{SHE}, hydrogen bonding increases the barrier of the second protonation step from 0.12 to 0.45 eV, although this barrier is still sufficiently low to be kinetically active at 298 K.

We also considered the effect of hydrogen bonding to an additional water molecule by adding a second explicit water in a position to hydrogen bond to *COOH, as shown in **Figure S2**. However, GC-DFT computes an additional stability of only 0.07 eV at -0.3 V_{SHE}, indicating that one explicit H_2O molecule combined with the implicit solvent sufficiently capture the effect of hydrogen bonding on the reaction energetics.

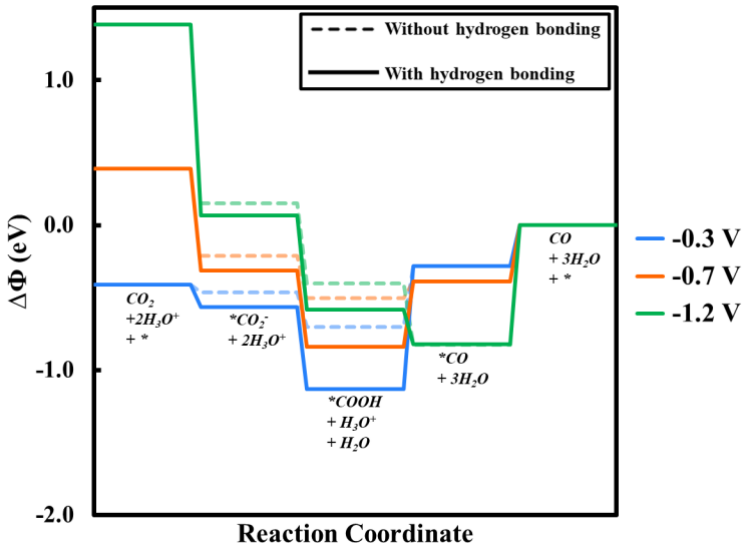

*Figure 5: Effect of hydrogen bonding to H_2O on the grand free energies of different reaction intermediates. The entropic contributions from vibrations of the adsorbates and the added explicit water molecule are included in the computed grand free energies. The dashed lines represent the reaction coordinate diagram without hydrogen bonding while solid lines include the stabilization resulting from hydrogen bonding to an explicit water molecule to adsorbed CO_2, COOH, and CO. *COOH is the most sensitive intermediate to hydrogen bonding and the added stability diminishes at more reducing potentials. *CO_2^- stabilization from hydrogen bonding is not affected by the applied potential. However, CO does not hydrogen bond with the solvating water molecules.*

The interaction of the reaction intermediates with explicit solvent molecules, such as through hydrogen bonding with H_2O, could affect their geometry and thus their binding to the Ti@4N-Gr site. Consequently, using an implicit solvent model could lead to inaccurate predictions of the PZC. We proposed a criterion above to choose the optimum applied potential range for the reduction of CO_2 to CO based on the PZC of *CO_2^- and *CO. To apply this criterion, it is important to evaluate how interactions with explicit solvent molecules affect the PZCs of the intermediates. **Table 1** shows the calculated PZCs with and without an explicit water molecule. Hydrogen bonding to H_2O only causes slight changes to the adsorbates' geometries and to their PZCs of up to 0.09 V. Although GC-DFT does not predict a significant change in the PZCs for these

intermediates, we still recommend that explicit solvent molecules be included for more accurate predictions of the PZCs.

*Table 1: Effect of including an explicit H_2O molecule hydrogen bonding to intermediates embedded in an implicit CANDLE solvent on their PZCs. The explicit water molecule slightly affects the intermediates' geometries and hence the PZCs of $*CO_2^-$, *COOH, and *CO adsorbed on Ti@4N-Gr.*

	PZC of Reaction Intermediates (V_{SHE})		
	$*CO_2^-$	***COOH**	***CO**
CANDLE	-0.22	-1.02	-0.84
Explicit H_2O in CANDLE	-0.22	-1.11	-0.75

Reaction Coordinate Diagrams for CO_2R Catalyzed by Ti@xN-Gr Defects

An important question that arises when analyzing conversions catalyzed by M@N-Gr catalysts is "what is the structure of the active site?" Nitrogen-doped graphene likely includes Ti@xN-Gr defect sites where x is 1, 2, or 3 and single Ti atoms are bound to nitrogen and carbon atoms instead of to the four nitrogen atoms of the Ti@4N-Gr site. Experimental characterization techniques do not clearly distinguish between neighboring carbon and nitrogen atoms.[74] Because the reaction energetics are likely sensitive to the Ti coordination, we computed the reaction energetics for CO_2R to CO at Ti@xN-Gr defects. We studied four possible Ti@xN-Gr defects; one configuration each for when x is 1 or 3, and the two possible configurations for when x is 2, where the two nitrogen atoms are on the same side (cis-Ti@2N-Gr) or on opposite sides (trans-Ti@2N-Gr) of the Ti center (see insets of **Figure 6**). **Figure 6** shows that $*CO_2^-$ is destabilized for the cases where Ti is coordinated to fewer nitrogen atoms. This results because the electronegativity of nitrogen is higher than that of carbon. This causes the Ti atom to be more positively charged when it is bound to more nitrogen atoms, which strengthens its bond with CO_2^-. GC-DFT also predicts a slight destabilization of the *COOH intermediate when Ti is coordinated to fewer N atoms at all potentials. However, GC-DFT predicts a significant destabilization of the *CO intermediate when

the Ti center is bound to fewer nitrogen atoms, which significantly lowers the desorption energy of CO. Nevertheless, the computed reaction energetics for CO_2R to CO conversion at Ti@xN-Gr defects predict that all defect configurations are thermodynamically promising catalytic sites at an applied potential of -0.7 V_{SHE}. However, they involve highly endergonic reactions for either *COOH protonation or *CO desorption at applied potentials of -0.3 and -1.2 V_{SHE}. Moreover, **Figure 6** shows that, at -0.7 V_{SHE}, the most likely mechanism for the first step of the CO_2R reaction is PCET instead of CO_2 adsorption over Ti@1N-Gr due to CO_2 adsorption being endergonic.

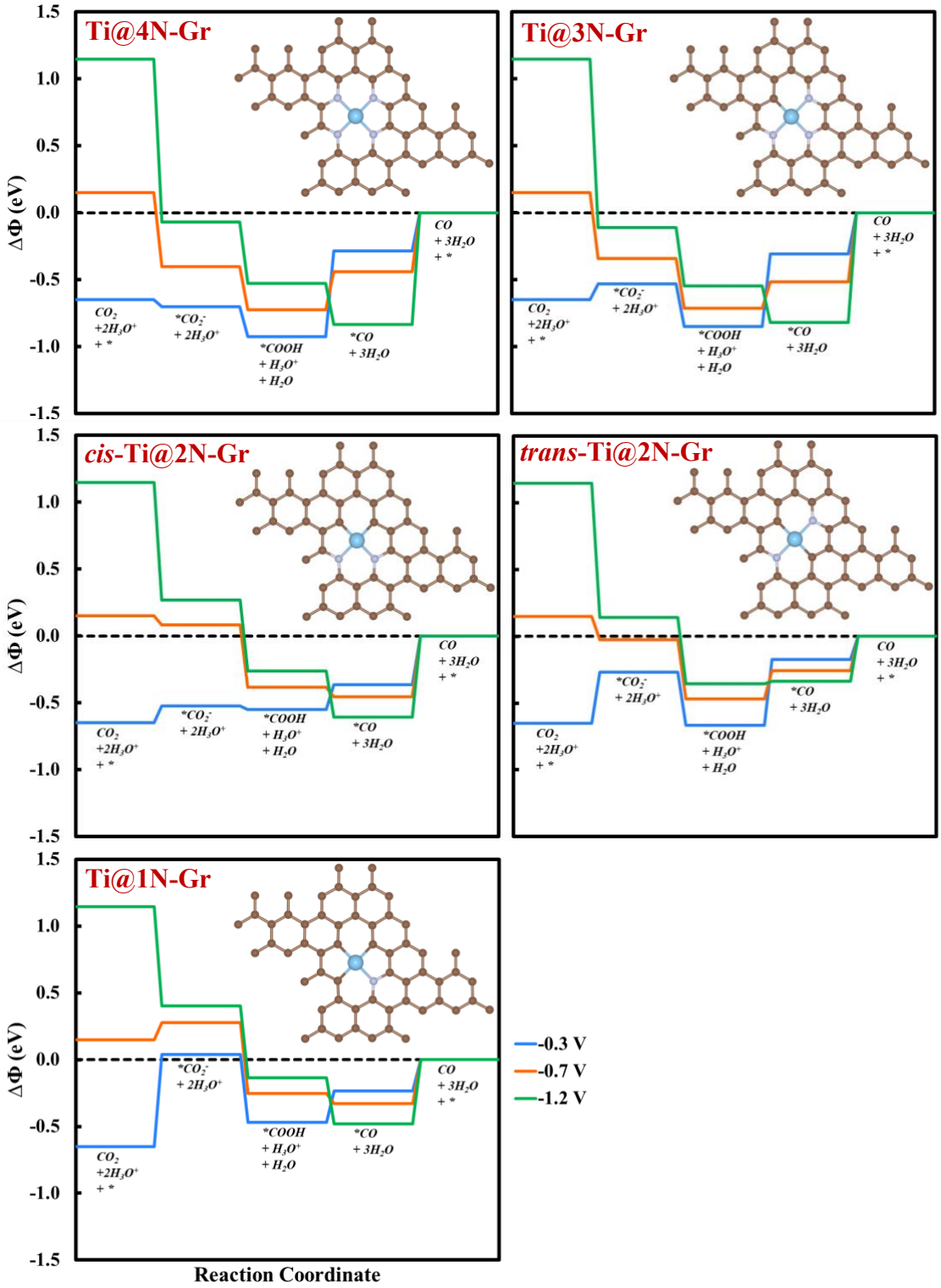

*Figure 6: Reaction coordinate diagrams for CO_2R to CO at Ti@4N-Gr and Ti@xN-Gr defects where x = 1, 2, or 3. The insets show the corresponding Ti@xN-Gr sites. These plots show that it is thermodynamically feasible to reduce CO_2 to CO at all sites at -0.7 V_{SHE} with reasonable energetic costs between intermediates. Ti@4N-Gr and Ti@3N-Gr are predicted to be poisoned by *CO at -1.2 V_{SHE}.*

Conclusion

CO_2R to CO using pyridinic M@N-Gr catalysts is promising due to its high Faradaic efficiency and CO selectivity. In this article, we report the results of GC-DFT calculations to further assess the performance of Ti@4N-Gr as an electrocatalyst for CO_2R to CO conversion. GC-NEB predicts a significant activation barrier of 1.02 eV for CO_2 adsorption at -0.3 V_{SHE}, which lowers to 0.74 eV at -1.2 V_{SHE}. However, GC-NEB predicts that *CO desorption has a large activation barrier that increases at more reducing potentials, indicating a case of an electrochemical reaction where the rate determining step (RDS) is potential dependent.

We proposed a criterion to choose the optimum applied potential range for CO_2R to CO based on the PZCs of $*CO_2^-$ and CO that can be calculated from canonical DFT. The optimum applied potential for CO_2R to CO lies in the range of $PZC_{*CO} < V < PZC_{*CO_2^-}$, provided that the geometries of $*CO_2^-$ and *CO do not change significantly with applied potential and CO adsorption becomes more favorable at more reducing potentials. The later condition can be assured by satisfying the condition that $PZC_* < PZC_{*CO}$. This criterion suggests that the optimum applied potential for CO_2R to CO over Ti@4N-Gr lies between -0.84 and -0.22 V.

The effect of hydrogen bonding on the energetics of the CO_2 to CO reduction catalyzed by Ti@4N-Gr was also investigated. $*CO_2^-$ gains moderate stability by hydrogen bonding with a solvating water molecule while *COOH forms strong hydrogen bonds with solvating water molecules, especially at more oxidizing potentials. On the other hand, GC-DFT predicts that *CO does not hydrogen bond to solvating water molecules.

This study demonstrates the importance of considering factors that could influence the rates of electrochemical reactions, such as defects that act as the active catalytic sites, hydrogen bonding

between reaction intermediates and solvated water molecules, and the effects of the applied potential on the thermodynamics and activation barriers of the reaction steps. Therefore, computational studies should consider these factors when investigating electrochemical reactions. Furthermore, the proposed criterion for choosing the optimum applied potential for CO_2R to CO should be investigated for a range of electrocatalysts, including 2d materials, pure metals, and alloys. A full kinetic study including all competing reactions at various reaction conditions, and microkinetic model with degree of rate control analysis[75-76] should be performed to further assess Ti@4N-Gr as a catalyst for CO_2R to CO reaction.

Supporting Information

Additional figures, results and descriptions of methods (PDF). This material is available free of charge via the Internet.

Acknowledgements

We gratefully acknowledge use of the Summit and Alpine supercomputers of the University of Colorado Boulder Research Computing Group, which are supported by the National Science Foundation (awards ACI-1532235 and ACI-1532236), the University of Colorado Boulder, and Colorado State University. We also thank King Fahd University of Petroleum and Minerals for financial support for YAA. CBM also acknowledge support from the U.S. Department of Energy, Office of Science, Basic Energy Sciences (DE-SC0022247) and from the U.S. National Science Foundation (CBET-2016225).

References

1. Friedlingstein, P.; Houghton, R. A.; Marland, G.; Hackler, J.; Boden, T. A.; Conway, T. J.; Canadell, J.; Raupach, M.; Ciais, P.; Le Quéré, C., Update on CO_2 Emissions. *Nature geoscience* **2010**, *3*, 811-812.
2. Wu, R.; Wang, J.; Wang, S.; Feng, K., The Drivers of Declining CO_2 Emissions Trends in Developed Nations Using an Extended Stirpat Model: A Historical and Prospective Analysis. *Renewable and Sustainable Energy Reviews* **2021**, *149*, 111328.
3. Ren, L.; Zhou, S.; Peng, T.; Ou, X., A Review of CO_2 Emissions Reduction Technologies and Low-Carbon Development in the Iron and Steel Industry Focusing on China. *Renewable and Sustainable Energy Reviews* **2021**, *143*, 110846.
4. Hoang, A. T.; Foley, A. M.; Nižetić, S.; Huang, Z.; Ong, H. C.; Ölçer, A. I.; Nguyen, X. P., Energy-Related Approach for Reduction of CO_2 Emissions: A Strategic Review on the Port-to-Ship Pathway. *Journal of Cleaner Production* **2022**, 131772.
5. Farooq, S.; Ozturk, I.; Majeed, M. T.; Akram, R., Globalization and CO_2 Emissions in the Presence of Ekc: A Global Panel Data Analysis. *Gondwana Research* **2022**, *106*, 367-378.
6. Gaies, B.; Nakhli, M. S.; Sahut, J.-M., What Are the Effects of Economic Globalization on CO_2 Emissions in Mena Countries? *Economic Modelling* **2022**, 106022.
7. Xie, J.; Zhou, Z.; Wang, Y., Metal–Co2 Batteries at the Crossroad to Practical Energy Storage and CO_2 Recycle. *Advanced Functional Materials* **2020**, *30*, 1908285.
8. Behzadi, A.; Habibollahzade, A.; Zare, V.; Ashjaee, M., Multi-Objective Optimization of a Hybrid Biomass-Based Sofc/Gt/Double Effect Absorption Chiller/Ro Desalination System with CO_2 Recycle. *Energy conversion and management* **2019**, *181*, 302-318.
9. Leonzio, G.; Zondervan, E.; Foscolo, P. U., Methanol Production by CO_2 Hydrogenation: Analysis and Simulation of Reactor Performance. *International Journal of Hydrogen Energy* **2019**, *44*, 7915-7933.
10. Zang, G.; Sun, P.; Elgowainy, A. A.; Bafana, A.; Wang, M., Performance and Cost Analysis of Liquid Fuel Production from H_2 and CO_2 Based on the Fischer-Tropsch Process. *Journal of* CO_2 *Utilization* **2021**, *46*, 101459.
11. Li, Y.; Wang, M.; Liu, X.; Hu, C.; Xiao, D.; Ma, D., Catalytic Transformation of Pet and CO_2 into High-Value Chemicals. *Angewandte Chemie* **2022**, *134*, e202117205.
12. Tsujiguchi, T.; Kawabe, Y.; Jeong, S.; Ohto, T.; Kukunuri, S.; Kuramochi, H.; Takahashi, Y.; Nishiuchi, T.; Masuda, H.; Wakisaka, M., Acceleration of Electrochemical CO_2 Reduction to Formate at the Sn/Reduced Graphene Oxide Interface. *Acs Catalysis* **2021**, *11*, 3310-3318.
13. Yi, Q.; Wu, G.-s.; Gong, M.-h.; Huang, Y.; Feng, J.; Hao, Y.-h.; Li, W.-y., A Feasibility Study for CO_2 Recycle Assistance with Coke Oven Gas to Synthetic Natural Gas. *Applied Energy* **2017**, *193*, 149-161.
14. Ma, J.; Sun, N.; Zhang, X.; Zhao, N.; Xiao, F.; Wei, W.; Sun, Y., A Short Review of Catalysis for CO_2 Conversion. *Catalysis Today* **2009**, *148*, 221-231.
15. Alper, E.; Orhan, O. Y., CO_2 Utilization: Developments in Conversion Processes. *Petroleum* **2017**, *3*, 109-126.
16. Song, C., CO_2 Conversion and Utilization: An Overview. **2002**.
17. Sullivan, I.; Goryachev, A.; Digdaya, I. A.; Li, X.; Atwater, H. A.; Vermaas, D. A.; Xiang, C., Coupling Electrochemical CO_2 Conversion with CO_2 Capture. *Nature Catalysis* **2021**, *4*, 952-958.

18. Abanades, J. C.; Alvarez, D., Conversion Limits in the Reaction of CO_2 with Lime. *Energy & Fuels* **2003**, *17*, 308-315.
19. Li, F.; Thevenon, A.; Rosas-Hernández, A.; Wang, Z.; Li, Y.; Gabardo, C. M.; Ozden, A.; Dinh, C. T.; Li, J.; Wang, Y., Molecular Tuning of CO_2-to-Ethylene Conversion. *Nature* **2020**, *577*, 509-513.
20. Rosen, B. A., A. Salehi-Khojin, Mr Thorson, W. Zhu, Dt Whipple, Pja Kenis and Ri Masel. *Science* **2011**, *334*, 643-644.
21. Saberi Safaei, T.; Mepham, A.; Zheng, X.; Pang, Y.; Dinh, C.-T.; Liu, M.; Sinton, D.; Kelley, S. O.; Sargent, E. H., High-Density Nanosharp Microstructures Enable Efficient CO_2 Electroreduction. *Nano letters* **2016**, *16*, 7224-7228.
22. Zhu, W.; Michalsky, R.; Metin, O. n.; Lv, H.; Guo, S.; Wright, C. J.; Sun, X.; Peterson, A. A.; Sun, S., Monodisperse Au Nanoparticles for Selective Electrocatalytic Reduction of CO_2 to CO. *Journal of the American Chemical Society* **2013**, *135*, 16833-16836.
23. Chen, Y.; Li, C. W.; Kanan, M. W., Aqueous CO_2 Reduction at Very Low Overpotential on Oxide-Derived Au Nanoparticles. *Journal of the American Chemical Society* **2012**, *134*, 19969-19972.
24. Tripkovic, V.; Vanin, M.; Karamad, M.; Björketun, M. r. E.; Jacobsen, K. W.; Thygesen, K. S.; Rossmeisl, J., Electrochemical CO_2 and CO Reduction on Metal-Functionalized Porphyrin-Like Graphene. *The Journal of Physical Chemistry C* **2013**, *117*, 9187-9195.
25. Yang, F.; Song, P.; Liu, X.; Mei, B.; Xing, W.; Jiang, Z.; Gu, L.; Xu, W., Highly Efficient CO_2 Electroreduction on Znn4-Based Single-Atom Catalyst. *Angewandte Chemie International Edition* **2018**, *57*, 12303-12307.
26. Chen, Z.; Mou, K.; Yao, S.; Liu, L., Zinc-Coordinated Nitrogen-Codoped Graphene as an Efficient Catalyst for Selective Electrochemical Reduction of CO_2 to CO. *ChemSusChem* **2018**, *11*, 2944-2952.
27. Li, J.; Pršlja, P.; Shinagawa, T.; Martin Fernandez, A. J.; Krumeich, F.; Artyushkova, K.; Atanassov, P.; Zitolo, A.; Zhou, Y.; García-Muelas, R., Volcano Trend in Electrocatalytic CO_2 Reduction Activity over Atomically Dispersed Metal Sites on Nitrogen-Doped Carbon. *ACS Catalysis* **2019**, *9*, 10426-10439.
28. Varela, A. S.; Kroschel, M.; Leonard, N. D.; Ju, W.; Steinberg, J.; Bagger, A.; Rossmeisl, J.; Strasser, P., Ph Effects on the Selectivity of the Electrocatalytic CO_2 Reduction on Graphene-Embedded Fe–N–C Motifs: Bridging Concepts between Molecular Homogeneous and Solid-State Heterogeneous Catalysis. *ACS Energy Letters* **2018**, *3*, 812-817.
29. Möller, T.; Ju, W.; Bagger, A.; Wang, X.; Luo, F.; Thanh, T. N.; Varela, A. S.; Rossmeisl, J.; Strasser, P., Efficient CO_2 to CO Electrolysis on Solid Ni–N–C Catalysts at Industrial Current Densities. *Energy & Environmental Science* **2019**, *12*, 640-647.
30. Lu, P.; Yang, Y.; Yao, J.; Wang, M.; Dipazir, S.; Yuan, M.; Zhang, J.; Wang, X.; Xie, Z.; Zhang, G., Facile Synthesis of Single-Nickel-Atomic Dispersed N-Doped Carbon Framework for Efficient Electrochemical CO_2 Reduction. *Applied Catalysis B: Environmental* **2019**, *241*, 113-119.
31. Su, P.; Iwase, K.; Nakanishi, S.; Hashimoto, K.; Kamiya, K., Nickel-Nitrogen-Modified Graphene: An Efficient Electrocatalyst for the Reduction of Carbon Dioxide to Carbon Monoxide. *Small* **2016**, *12*, 6083-6089.
32. Yan, C.; Li, H.; Ye, Y.; Wu, H.; Cai, F.; Si, R.; Xiao, J.; Miao, S.; Xie, S.; Yang, F., Coordinatively Unsaturated Nickel–Nitrogen Sites Towards Selective and High-Rate CO_2 Electroreduction. *Energy & Environmental Science* **2018**, *11*, 1204-1210.

33. Nørskov, J. K.; Rossmeisl, J.; Logadottir, A.; Lindqvist, L.; Kitchin, J. R.; Bligaard, T.; Jonsson, H., Origin of the Overpotential for Oxygen Reduction at a Fuel-Cell Cathode. *The Journal of Physical Chemistry B* **2004**, *108*, 17886-17892.
34. Hansen, H. A.; Varley, J. B.; Peterson, A. A.; Nørskov, J. K., Understanding Trends in the Electrocatalytic Activity of Metals and Enzymes for CO_2 Reduction to CO. *The journal of physical chemistry letters* **2013**, *4*, 388-392.
35. Durand, W. J.; Peterson, A. A.; Studt, F.; Abild-Pedersen, F.; Nørskov, J. K., Structure Effects on the Energetics of the Electrochemical Reduction of CO_2 by Copper Surfaces. *Surface Science* **2011**, *605*, 1354-1359.
36. Peterson, A. A.; Abild-Pedersen, F.; Studt, F.; Rossmeisl, J.; Nørskov, J. K., How Copper Catalyzes the Electroreduction of Carbon Dioxide into Hydrocarbon Fuels. *Energy & Environmental Science* **2010**, *3*, 1311-1315.
37. Guo, L.; Guo, S., Mechanistic Understanding of CO_2 Reduction Reaction Towards C_1 Products by Molecular Transition Metal Porphyrin Catalysts. *International Journal of Hydrogen Energy* **2021**, *46*, 10608-10623.
38. Zhang, Y.; Fang, L.; Cao, Z., Atomically Dispersed Cu and Fe on N-Doped Carbon Materials for CO_2 Electroreduction: Insight into the Curvature Effect on Activity and Selectivity. *RSC Advances* **2020**, *10*, 43075-43084.
39. Chan, K., A Few Basic Concepts in Electrochemical Carbon Dioxide Reduction. *Nature Communications* **2020**, *11*, 1-4.
40. Alfonso, D. R., CO_2 Conversion on Ligand-Protected Au_{25} Nanoparticle: The Role of Structural Inhomogeneity in the Promotion of the Electrocatalytic Process. *physica status solidi (b)* **2021**, *258*, 2000387.
41. Rendon-Calle, A.; Builes, S.; Calle-Vallejo, F., A Brief Review of the Computational Modeling of CO_2 Electroreduction on Cu Electrodes. *Current Opinion in Electrochemistry* **2018**, *9*, 158-165.
42. Alsunni, Y. A.; Alherz, A. W.; Musgrave, C. B., Electrocatalytic Reduction of CO_2 to CO over Ag (110) and Cu (211) Modeled by Grand-Canonical Density Functional Theory. *The Journal of Physical Chemistry C* **2021**, *125*, 23773-23783.
43. Brimley, P.; Almajed, H.; Alsunni, Y.; Alherz, A. W.; Bare, Z. J.; Smith, W. A.; Musgrave, C. B., Electrochemical CO_2 Reduction over Metal-/Nitrogen-Doped Graphene Single-Atom Catalysts Modeled Using the Grand-Canonical Density Functional Theory. *ACS Catalysis* **2022**, *12*, 10161-10171.
44. Schwarz, K.; Sundararaman, R., The Electrochemical Interface in First-Principles Calculations. *Surface science reports* **2020**, *75*, 100492.
45. Sundararaman, R.; Schwarz, K., Evaluating Continuum Solvation Models for the Electrode-Electrolyte Interface: Challenges and Strategies for Improvement. *The Journal of chemical physics* **2017**, *146*, 084111.
46. Melander, M. M.; Kuisma, M. J.; Christensen, T. E. K.; Honkala, K., Grand-Canonical Approach to Density Functional Theory of Electrocatalytic Systems: Thermodynamics of Solid-Liquid Interfaces at Constant Ion and Electrode Potentials. *The Journal of chemical physics* **2019**, *150*.
47. Hörmann, N. G.; Andreussi, O.; Marzari, N., Grand Canonical Simulations of Electrochemical Interfaces in Implicit Solvation Models. *The Journal of chemical physics* **2019**, *150*.

48. Schwarz, K.; Sundararaman, R., The Electrochemical Interface in First-Principles Calculations. *Surface Science Reports* **2020**, 100492.
49. Shen, Q.; Huang, L.; Chen, G.; Zhang, X.; Chen, Y., One-Step Synthesis of Titanium Nitride/Nitrogen-Doped Graphene Nanocomposite as Separator Modifying Material for Advanced Lithium-Sulfur Batteries. *Journal of Alloys and Compounds* **2020**, *845*, 155543.
50. Li, S.; Zhao, H.-m.; Jena, P., Ti-Doped Nano-Porous Graphene: A Material for Hydrogen Storage and Sensor. *Frontiers of Physics* **2011**, *6*, 204-208.
51. Liu, L.-L.; Chen, C.-P.; Zhao, L.-S.; Wang, Y.; Wang, X.-C., Metal-Embedded Nitrogen-Doped Graphene for H_2O Molecule Dissociation. *Carbon* **2017**, *115*, 773-780.
52. Esrafili, M. D.; Mohammadian-Sabet, F.; Nematollahi, P., Oxidation of CO by N_2O over Al-and Ti-Doped Graphene: A Comparative Study. *RSC advances* **2016**, *6*, 64832-64840.
53. Esrafili, M. D.; Dinparast, L., A Dft Study on the Catalytic Hydrogenation of CO_2 to Formic Acid over Ti-Doped Graphene Nanoflake. *Chemical Physics Letters* **2017**, *682*, 49-54.
54. Zhang, Z.; Liang, B.; Chi, Y.; Jiang, Y.; Song, J.; Guo, Y., Adsorption Mechanism of SO_2 on Vacancy-Defected Graphene and Ti Doped Graphene: A Dft Study. *Superlattices and Microstructures* **2021**, *159*, 107036.
55. Luo, Q.; Yin, S.; Sun, X.; Tang, Y.; Feng, Z.; Dai, X., Density Functional Theory Study on the Adsorption Properties of SO_2 Gas on Graphene, N, Ti, and N–Ti Doped Graphene. *Micro and Nanostructures* **2022**, *171*, 207401.
56. Yan, Z.; Bai, Y.; Sun, L., Adsorption of Thiophene and Sox Molecules on Cr-Doped and Ti-Doped Graphene Nanosheets: A Dft Study. *Materials Research Express* **2019**, *6*, 125067.
57. Singstock, N. R.; Musgrave, C. B., How the Bioinspired $Fe_2Mo_6S_8$ Chevrel Breaks Electrocatalytic Nitrogen Reduction Scaling Relations. *Journal of the American Chemical Society* **2022**, *144*, 12800-12806.
58. Ong, S. P.; Richards, W. D.; Jain, A.; Hautier, G.; Kocher, M.; Cholia, S.; Gunter, D.; Chevrier, V. L.; Persson, K. A.; Ceder, G., Python Materials Genomics (Pymatgen): A Robust, Open-Source Python Library for Materials Analysis. *Computational Materials Science* **2013**, *68*, 314-319.
59. Sundararaman, R.; Letchworth-Weaver, K.; Schwarz, K. A.; Gunceler, D.; Ozhabes, Y.; Arias, T., Jdftx: Software for Joint Density-Functional Theory. *SoftwareX* **2017**, *6*, 278-284.
60. Sundararaman, R.; Goddard III, W. A., The Charge-Asymmetric Nonlocally Determined Local-Electric (Candle) Solvation Model. *The Journal of chemical physics* **2015**, *142*, 064107.
61. Sundararaman, R.; Goddard, W. A.; Arias, T. A., Grand Canonical Electronic Density-Functional Theory: Algorithms and Applications to Electrochemistry. *The Journal of chemical physics* **2017**, *146*.
62. Larsen, A. H.; Mortensen, J. J.; Blomqvist, J.; Castelli, I. E.; Christensen, R.; Dułak, M.; Friis, J.; Groves, M. N.; Hammer, B.; Hargus, C., The Atomic Simulation Environment—a Python Library for Working with Atoms. *Journal of Physics: Condensed Matter* **2017**, *29*, 273002.
63. Mills, G.; Jónsson, H., Quantum and Thermal Effects in H_2 Dissociative Adsorption: Evaluation of Free Energy Barriers in Multidimensional Quantum Systems. *Physical review letters* **1994**, *72*, 1124.
64. Henkelman, G.; Uberuaga, B. P.; Jónsson, H., A Climbing Image Nudged Elastic Band Method for Finding Saddle Points and Minimum Energy Paths. *The Journal of chemical physics* **2000**, *113*, 9901-9904.
65. Shi, Z.; Yang, W.; Gu, Y.; Liao, T.; Sun, Z., Metal-Nitrogen-Doped Carbon Materials as Highly Efficient Catalysts: Progress and Rational Design. *Advanced Science* **2020**, *7*, 2001069.

66. Abidi, N.; Steinmann, S. N., How Are Transition States Modeled in Heterogeneous Electrocatalysis? *Current Opinion in Electrochemistry* **2022**, *33*, 100940.
67. Qin, X.; Hansen, H. A.; Honkala, K.; Melander, M. M., Cation-Induced Changes in the Inner-and Outer-Sphere Mechanisms of Electrocatalytic CO_2 Reduction. *Nature Communications* **2023**, *14*, 7607.
68. Shinagawa, T.; Garcia-Esparza, A. T.; Takanabe, K., Mechanistic Switching by Hydronium Ion Activity for Hydrogen Evolution and Oxidation over Polycrystalline Platinum Disk and Platinum/Carbon Electrodes. *ChemElectroChem* **2014**, *1*, 1497-1507.
69. Zeitler, E. L.; Ertem, M. Z.; Pander, J. E.; Yan, Y.; Batista, V. S.; Bocarsly, A. B., Isotopic Probe Illuminates the Role of the Electrode Surface in Proton Coupled Hydride Transfer Electrochemical Reduction of Pyridinium on Pt (111). *Journal of The Electrochemical Society* **2015**, *162*, H938.
70. Seifitokaldani, A.; Gabardo, C. M.; Burdyny, T.; Dinh, C.-T.; Edwards, J. P.; Kibria, M. G.; Bushuyev, O. S.; Kelley, S. O.; Sinton, D.; Sargent, E. H., Hydronium-Induced Switching between CO_2 Electroreduction Pathways. *Journal of the American Chemical Society* **2018**, *140*, 3833-3837.
71. Abidi, N.; Bonduelle-Skrzypczak, A.; Steinmann, S. N., Potential and Support-Dependent Hydrogen Evolution Reaction Activation Energies on Sulfur Vacancies of MoS_2 from Gc-Dft. *International Journal of Hydrogen Energy* **2023**, *48*, 8478-8488.
72. Hanslin, S. Ø.; Jónsson, H.; Akola, J., Sulfur-Deficient Edges as Active Sites for Hydrogen Evolution on MoS_2. *Physical Chemistry Chemical Physics* **2023**, *25*, 32541-32548.
73. Zhao, X.; Liu, Y., Unveiling the Active Structure of Single Nickel Atom Catalysis: Critical Roles of Charge Capacity and Hydrogen Bonding. *Journal of the American Chemical Society* **2020**, *142*, 5773-5777.
74. Luo, Z.; Yin, Z.; Yu, J.; Yan, Y.; Hu, B.; Nie, R.; Kolln, A. F.; Wu, X.; Behera, R. K.; Chen, M., General Synthetic Strategy to Ordered Mesoporous Carbon Catalysts with Single-Atom Metal Sites for Electrochemical CO_2 Reduction. *Small* **2022**, *18*, 2107799.
75. Campbell, C. T., The Degree of Rate Control: A Powerful Tool for Catalysis Research. ACS Publications: 2017; Vol. 7, pp 2770-2779.
76. Campbell, C. T., Finding the Rate-Determining Step in a Mechanism: Comparing Dedonder Relations with the "Degree of Rate Control". Elsevier: 2001; Vol. 204, pp 520-524.

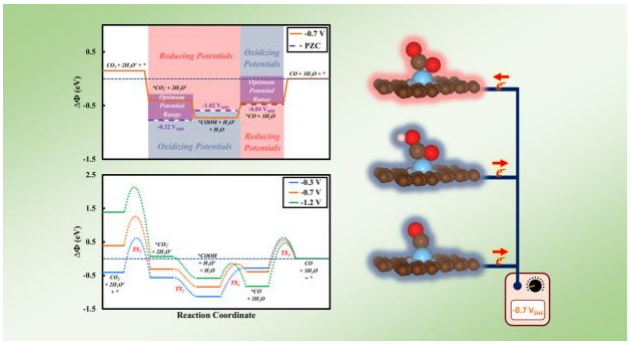
-0.7 V
PZC
Reducing Potentials
Oxidizing Potentials
Optimum Potential Range
Oxidizing Potentials
Reducing Potentials
-1.03 V_SHE
-0.22 V_SHE
-0.83 V_SHE
ΔΦ (eV)
0.5
-0.5
-1.5
-0.3 V
-0.7 V
-1.2 V
2.5
1.5
0.5
-0.5
-1.5
Reaction Coordinate
-0.7 V_SHE